

Article

# Divergent Sensitivities of Spaceborne Solar-Induced Chlorophyll Fluorescence to Drought among Different Seasons and Regions

Xiaofang Sun <sup>1,2</sup> , Meng Wang <sup>1,\*</sup>, Guicai Li <sup>3</sup>, Junbang Wang <sup>2</sup> and Zemeng Fan <sup>2</sup>

<sup>1</sup> School of Geography and Tourism, Qufu Normal University, Rizhao 276800, China; sunxf@qfnu.edu.cn

<sup>2</sup> Institute of Geographical Science and Natural Resources Research, Chinese Academy of Sciences, Beijing 100101, China; wangjb@igsnr.ac.cn (J.W.); fanzm@lreis.ac.cn (Z.F.)

<sup>3</sup> National Satellite Meteorological Center, China Meteorological Administration, Beijing 100081, China; guicai\_li@163.com

\* Correspondence: wangmeng@qfnu.edu.cn

Received: 21 July 2020; Accepted: 7 September 2020; Published: 9 September 2020



**Abstract:** As a newly emerging satellite form of data, solar-induced chlorophyll fluorescence (SIF) provides a direct measurement of photosynthetic activity. The potential of SIF for drought assessment in different grassland ecosystems is not yet clear. In this study, the correlations between spaceborne SIF and nine drought indices were evaluated. Standardized precipitation evapotranspiration index (SPEI) at a 1, 3, 6, 9, 12 month scale, Palmer drought severity index (PDSI), soil moisture, temperature condition index (TCI), and vapor pressure deficit (VPD) were evaluated. The relationships between different grassland types and different seasons were compared, and the driving forces affecting the sensitivity of SIF to drought were explored. We found that the correlations between SIF and drought indices were different for temperate grasslands and alpine grasslands. The correlation coefficients between SIF and soil moisture were the highest (the mean value was 0.72 for temperate grasslands and 0.69 for alpine grasslands), followed by SPEI and PDSI at a three month scale, and the correlation coefficient between SIF and TCI was the lowest (the mean value was 0.38 for both temperate and alpine grasslands). Spaceborne SIF is more effective for drought monitoring during the peak period of the growing season (July and August). Temperature and radiation are important factors affecting the sensitivity of SIF to drought. The results from this study demonstrated the importance of SIF in drought monitoring especially for temperate grasslands in the peak growing season.

**Keywords:** solar-induced fluorescence; drought; temperate and alpine grassland

## 1. Introduction

Drought influences the functions of the terrestrial ecosystem and the carbon budget [1]. Several studies have highlighted the negative impact of drought on groundwater availability [2,3], agricultural production and food security [4,5], ecosystem net primary production [6], and socio-economic status [7]. These impacts are projected to be exacerbated under the current and future changing climate [8]. Therefore, it is important to understand and monitor the behavior of this phenomenon in order to accurately plan for adaptation and mitigation strategies.

Drought can impact vegetation photosynthesis in both physical (i.e., vegetation greenness) and physiological (i.e., stomatal responses) pathways, which differs in terms of time scale and the process involved [9]. The drought impact on vegetation greenness can be reflected by vegetation indices (VIs). The change in vegetation greenness causes a reduction in absorbed photosynthetic active radiation (APAR), which may take effect at the time scale of days. However, the physiological functions impacted by drought can occur in time scale of hours to days. Over the last decades, the traditional

VIs, such as the normalized difference vegetation index (NDVI), were in widespread use for drought monitoring [10–13]. However, it is difficult for traditional VIs to manifest the accurate response of an ecosystem to drought. The reason for this is that they are able to indicate the potential photosynthetic ability instead of the actual condition. Moreover, some VIs have been detected showing a delayed response to drought [14–20].

During the process of photosynthesis, about 1–2% of the energy absorbed by chlorophyll is re-emitted at longer wavelengths as fluorescence, which is called solar-induced chlorophyll fluorescence (SIF) [14,21]. The physical and physiological responses of plants to drought can be mirrored in SIF and reduce the magnitude of reflected fluorescence [21]. Therefore, SIF provides a new way of estimating photosynthesis activity and has a closer relationship to the photosynthesis process than VIs.

The important role of meteorological factors, such as precipitation [22], temperature [23], and evapotranspiration [24,25], in drought analysis has been well established in the literature. Accordingly, several indices have been developed to account for the timing and magnitude of drought incident; for example, the standardized precipitation evapotranspiration index (SPEI) [26], Palmer drought severity index (PDSI) [27], and temperature condition index (TCI) [28]. However, the relationship between these indices and SIF has remained uncertain given its dependency on vegetation type and regional climate.

In recent years, SIF has been explored as a novel approach to estimate photosynthesis, which is closely related to gross primary production (GPP) and can respond rapidly to drought [29–31]. Several studies demonstrated that SIF responds earlier than VIs to water deficits, and SIF also showed more sensitivity to drought than VIs [15,29,31–33]. Ni et al. (2018) compared the sensitivity of SIF, GPP, NDVI and land surface temperature (LST) to drought. The results illustrated that SIF is highly sensitive and has earlier responses than GPP, NDVI, and land surface temperature (LST) in the condition of drought [34]. Chen et al. (2019) explored the ability of satellite-borne SIF in drought assessment and found that the regional averaged SIF declined more than NDVI and land surface water index (LSWI). They also found that the relationship between GPP and SIF was more significant than that between GPP and NDVI [35]. Wang et al. (2019) showed that SIF can capture the spatiotemporal pattern of the drought process, and SIF demonstrated a significant reduction and earlier response than EVI [19].

Previous studies have reported the feasibility of satellite-borne SIF in drought monitoring. However, previous studies have mostly investigated SIF related to drought [36] and explored whether SIF is superior in drought monitoring compared with traditional VIs. Few attempts have been made to find out the difference of the sensitivity of SIF to drought between different ecosystems. The spatiotemporal pattern of the feasibility of SIF to monitor drought among different vegetation types remains poorly understood. Some studies have looked at SIF in different seasons, some studies have looked at SIF seasonality for different vegetation [37], but studies have not focused on or evaluated SIF as a drought monitoring tool for grasslands across seasons.

The arid and semiarid zone of China, a region mostly dominated by temperate grasslands and alpine grasslands, includes important ecosystems in livestock production and climate change mitigation. These two grassland ecosystems have increased drought suppression over the past decades. The temperate grasslands and alpine grasslands have different mechanisms in the adaptability to environmental stress. The difference in the response of SIF to drought between temperate grasslands and alpine grasslands deserves further research. Whether the seasonality of the SIF sensitivity to drought exists in the two typical grasslands is still unclear. In an effort to address these issues, this study attempts to answer these three questions:

- (1) do the responses of SIF to drought indices show a consistent pattern between temperate grasslands and alpine grasslands?
- (2) How do the sensitivities of SIF to different drought indices shift in different seasons?
- (3) What are the main drivers influencing the relationship between SIF and drought indices?

## 2. Materials and Methods

### 2.1. Study Region

The study area located in northern China covers 47% of China's territorial area, which is the arid and semiarid zone of China. The arid and semiarid zone is defined as the area with a ratio of precipitation to evapotranspiration smaller than 0.5. It ranges from 73°29' to 125°51' longitude and from 27°14' to 50°08' latitude, covering a total area of  $4.6 \times 10^6$  km<sup>2</sup> and falling within 12 provinces [38]. The average altitude of the study area is 2530 m. The major ecosystem types are grasslands and deserts. The grasslands include temperate grasslands and alpine grasslands (Figure 1). The temperate grasslands are mainly located in Inner Mongolia and the Loess Plateau with an average elevation of 1200 m, and the alpine grasslands are mainly located in the Tibetan Plateau with an average elevation of more than 4000 m above sea level. These grasslands are different in climate, plant species and soil properties [39]. The growing season is from April to October for temperate grassland, and from May to September for alpine grassland [40]. To facilitate analysis and comparison, we selected the months from April to October as the research period. The extents of the temperate and alpine grasslands were extracted from a 1:1 million China vegetation map. Meanwhile, pixels with a multiyear mean NDVI < 0.1 were excluded to eliminate the impact of sparsely vegetated areas [41]. Here, the mean NDVI was calculated by averaging the monthly NDVI during 2007–2018.

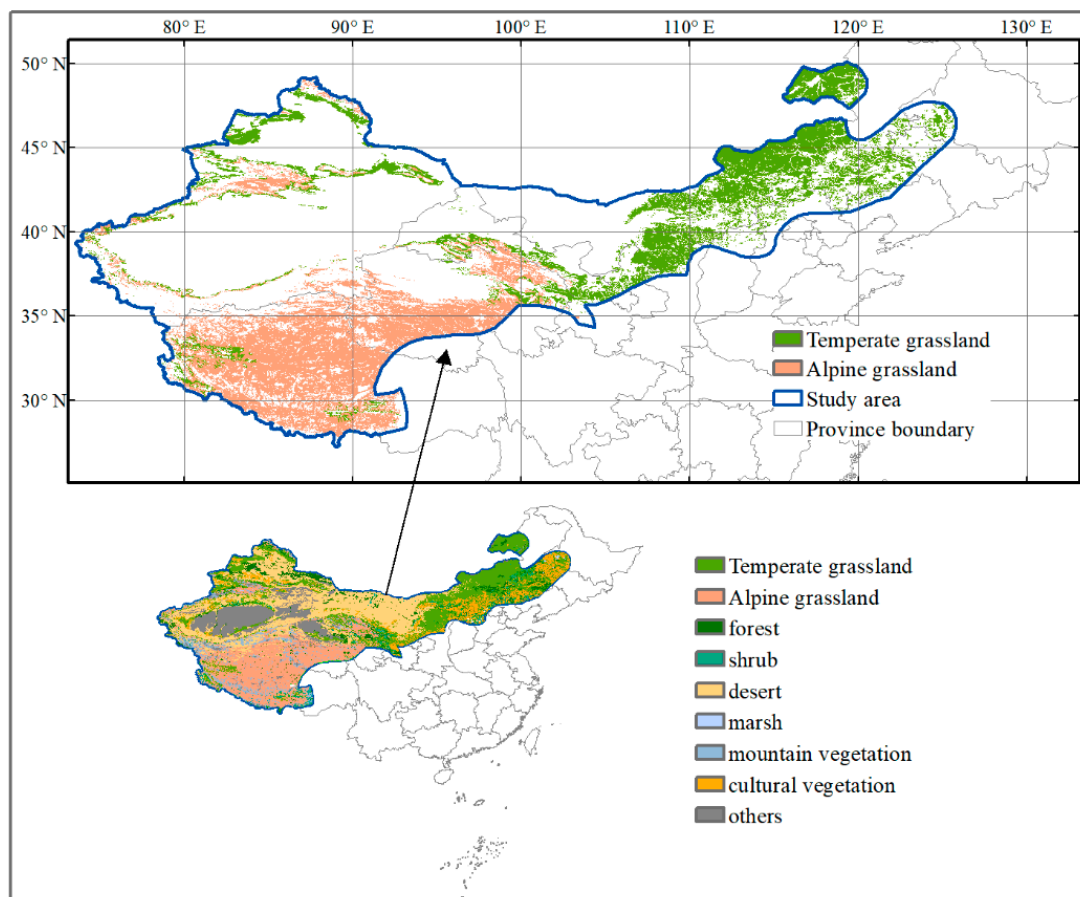


Figure 1. Geographic location of the study area.

## 2.2. Data

### 2.2.1. Satellite Chlorophyll Fluorescence Data

SIF is emitted by plants as a by-product of photosynthesis. The SIF signal has been shown to approximate photosynthetic activities. It is based on the theory that chlorophyll of plants emits fluorescence in the near infrared range during the photosynthesis process [21,42]. Large-scale photosynthetic activities can be derived by space borne measurements of SIF. In this study, satellite SIF data from the Monitoring Experiment-2 (GOME-2) instrument on MetOp-A platform were used. The SIF at 740 nm was retrieved from a spectral range between 720 and 758 nm with an algorithm, which reduced both the retrieval noise and the sensitivity of the SIF retrieval to cloud contamination [43]. A monthly gridded SIF product at  $0.5^\circ$  latitude  $\times 0.5^\circ$  longitude resolution from 2007 to 2018 was applied in our study.

### 2.2.2. Drought Dataset

Drought indices reflect different aspects of drought. SPEI has been widely used because it is statistically robust and due to its multi-scalar characteristics [44]. The SPEI calculated for 1, 3, 6, 9, and 12 month timescales would be used to examine the response of SIF to cumulative meteorological drought ranging from 1 to 12 months. The timescale refers to the period in which antecedent climate conditions are accumulated. Monthly PDSI from 2007 to 2018 was used to represent the balance condition of temperature, potential evapotranspiration, and precipitation of the study area [45,46].

The soil moisture data were derived from the Climate Change Initiative (CCI) of the European Space Agency (ESA). The ESA CCI SM v04.2 soil moisture product was used in this study. It was merged from the retrievals of 13 active and passive sensors [47–49]. The daily mean surface soil moisture datasets at a spatial resolution of  $0.25^\circ$  are available from 2007 to 2018. In this study, the soil moisture was collated into monthly soil moisture using the average of daily data. These datasets have been proven to be consistent with in situ soil moisture observations.

The monthly mean air temperature ( $^\circ\text{C}$ ) and relative humidity (%) data in the Global Land Data Assimilation Systems (GLDAS) from 2007 to 2018 were used to calculate the vapor pressure deficit (VPD) using the following formulas:

$$e^s = 0.611 \times e^{17.27 \times \frac{T}{273.3+T}} \quad (1)$$

$$VPD = (1 - RH/100) \times e^s \quad (2)$$

where  $e^s$  is saturated vapor pressure, RH is relative humidity (%), and  $T$  is temperature ( $^\circ\text{C}$ ).

The MODIS LST product MOD11C3 with 8 day temporal resolution and 500 m spatial resolution from 2007 to 2018 was obtained from the Land Processes Distributed Active Center. The night LST was extracted and combined into monthly LST using the number of days in each month as weight [50]. Then the Temperature Condition Index (TCI) was estimated from the monthly night LST data and can be formulated as:

$$TCI_i = \frac{LST_{i,max} - LST_i}{LST_{i,max} - LST_{i,min}} \quad (3)$$

where  $LST_{i,max}$  and  $LST_{i,min}$  are the maximum night LST and minimum night LST in month  $i$ , respectively.

### 2.2.3. Vegetation Type Data and Ancillary Data

The spatial distribution of temperate grasslands and alpine grasslands were derived from the 1:1 million China vegetation map (Editorial Board of Vegetation Map of China 2001). The temperate and alpine grasslands within the arid and semiarid zone were extracted.

To understand the factors influencing the sensitivity of SIF data to drought, eight potential driving factors were investigated. These include the historical climate data during the growing season (mean

temperature, maximum temperature, minimum temperature, and mean precipitation), historical mean GPP data during the growing season, digital elevation model (DEM) data, historical mean radiation data during the growing season, and historical mean LST data during the growing season. The gridded historical climate data were obtained from the National Meteorological Information Center, China Meteorological Data Service Center. These monthly climate surfaces were derived by the thin-plate-spline method from ANUSPLIN software using data from 2472 weather stations. The historical mean growing season climate data layers were calculated using 12 year (2007–2018) 10 month (during April and October) data. The growing season mean GPP data were calculated from the monthly MODIS GPP dataset (MOD17A2).

We integrated all the data used in this study (Table 1) into the same spatial resolution as the SIF data using the BILINEAR resample technique based on ArcPy. All data pre-processing and statistical analyses were conducted in Python version 2.7.

**Table 1.** Details of collected datasets used in this study.

Variable	Temporal Resolution	Spatial Resolution	Source
SIF	monthly	0.5-degree	<a href="ftp://fluo.gps.caltech.edu/data/Philipp/GOME-2/">ftp://fluo.gps.caltech.edu/data/Philipp/GOME-2/</a>
SPEI	monthly	0.5-degree	<a href="http://spei.csic.es/database.html">http://spei.csic.es/database.html</a>
PDSI	monthly	0.5-degree	<a href="https://crudata.uea.ac.uk/cru/data/drought/#global">https://crudata.uea.ac.uk/cru/data/drought/#global</a>
LST (MOD11C3)	8-day	500 m	<a href="https://search.earthdata.nasa.gov">https://search.earthdata.nasa.gov</a>
VPD	monthly	0.25-degree	<a href="https://disc.gsfc.nasa.gov/">https://disc.gsfc.nasa.gov/</a>
Soil moisture	daily	0.25-degree	<a href="https://www.esa-soilmoisture-cci.org/node/227">https://www.esa-soilmoisture-cci.org/node/227</a>
Climatic data	monthly	Point-based	<a href="http://data.cma.cn/en">http://data.cma.cn/en</a>
GPP (MOD11C3)	monthly	1000 m	<a href="https://search.earthdata.nasa.gov">https://search.earthdata.nasa.gov</a>
Radiation data	monthly	1-degree	<a href="https://ceres.larc.nasa.gov/data/">https://ceres.larc.nasa.gov/data/</a>
DEM	-	1000 m	<a href="http://www.resdc.cn/">http://www.resdc.cn/</a>

### 2.3. Statistical Analysis

The correlation coefficients (*r* values) between SIF and drought variables (SPEI-1, SPEI-3, SPEI-6, SPEI-9, SPEI-12, PDSI, TCI), soil moisture, and VPD were used to assess the ability of spaceborne SIF to monitor drought across the study area.

$$r = \frac{\sum (x_{i,j} - \bar{x}) \times \sum (y_{i,j} - \bar{y})}{\sqrt{\sum (x_{i,j} - \bar{x})^2 \times \sum (y_{i,j} - \bar{y})^2}} \quad (4)$$

here,  $x_{i,j}$  and  $y_{i,j}$  are the values of pixel ( $i, j$ ), and  $\bar{x}$  and  $\bar{y}$  are the mean value of pixel ( $i, j$ ) from the year 2007 to 2018.

The correlation coefficients were evaluated independently for each month of the growing season. The *r* value between SIF and SPEIs, PDSI, TCI, VPD, and soil moisture at each pixel level was calculated to understand the relationship between them. The differences in the sensitivity of SIF to drought conditions between temperate grasslands and alpine grasslands were compared. All data processing and statistical analyses were performed in Python version 2.7 (<https://www.python.org/>).

Furthermore, the random forest (RF) method was applied to estimate the importance of the factors influencing the relationship between SIF and drought indices, soil moisture, and VPD. The percentage increase in the mean squared error (%IncMSE) was calculated using the RF algorithm to evaluate the variable importance. The RF regression method was performed using the “randomForest” R package (<https://www.r-project.org/>) [51]. The 8 driving factors described in Section 2.2.3 (mean temperature, maximum temperature, minimum temperature, precipitation, GPP, radiation, LST during the growing season, and DEM) were used as explanatory variables, and the coefficients of correlation between spaceborne SIF and drought indices were used as dependent variables. In this study, 500 binary decision trees were included, and each node was split using the best split among all covariates.

### 3. Results

#### 3.1. Correlations between SIF and SPEI at Different Time Scales

Each record in Figure 2 is the correlation coefficients between SIF and SPEIs for one grid cell. For each grid cell, correlation analysis was performed taking SIF and SPEI during 2007 and 2018 as the x and y variable, respectively. All the presented correlation coefficients in Figure 2 are statistically significant ( $p$  values  $< 0.05$ ). The  $r$  values between SIF and SPEI at different time scales for temperate grasslands and alpine grasslands were compared. For the temperate grassland, the correlation coefficients between SIF and 1, 3, 6, 9, and 12 month SPEI were higher in July and August than other months. However, for the alpine grassland, the correlation coefficients between SIF and the SPEIs were higher in June and July than other months. At all the time scales, the  $r$  values between SIF and SPEI were higher for temperate grasslands than alpine grasslands (Figure 2). Within the 1, 3, 6, 9, and 12 month time scales, the correlations between the SIF and three month SPEI (SPEI-3) were slightly higher than SPEI at other time scales. There were no significant differences between SPEI-3 and longer-term SPEIs.

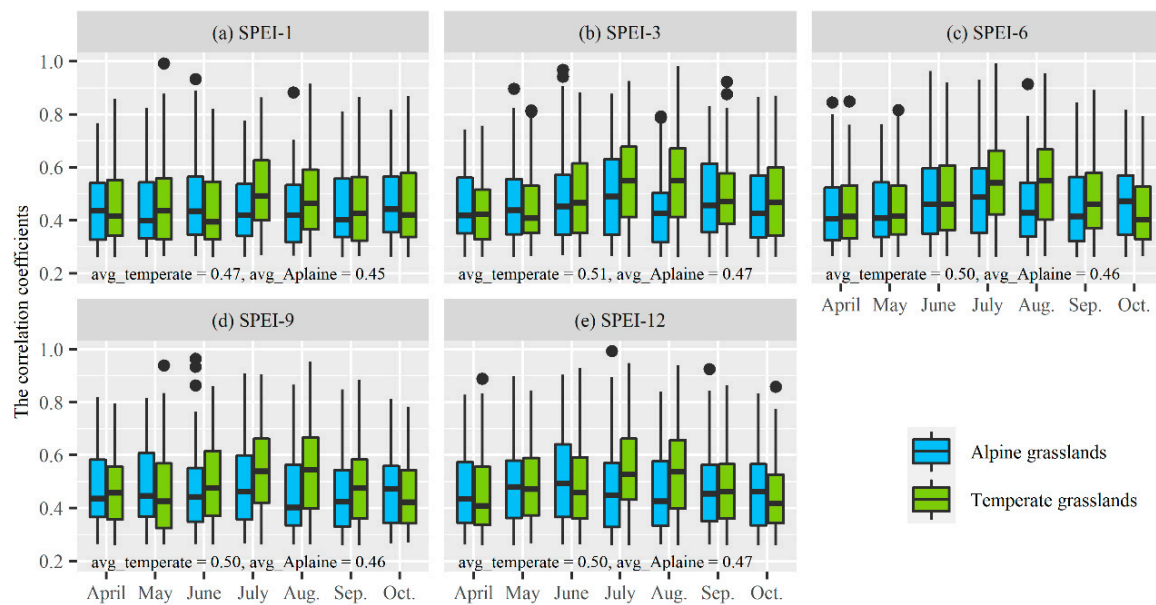


**Figure 2.** The  $r$  values between solar-induced chlorophyll fluorescence (SIF) and standardized precipitation evapotranspiration index (SPEI) for temperate grasslands and alpine grasslands under 1 month (a), 3 months (b), 6 months (c), 9 months (d), and 12 months (e). All the reported correlation coefficients are statistically significant ( $p$  values  $< 0.05$ ).

The spatial pattern of the correlation coefficients between the SIF and SPEI-3 was calculated from April to October at pixel level between 2007 and 2018 (Figure 3). As depicted, the spatial pattern of the correlation coefficients between SIF and SPEI-3 were similar in the early growing season (April and May) and late growing season (October). However, in July and August, the pixels with an  $r$  value larger than 0.5 were distributed mainly in the temperature grassland.

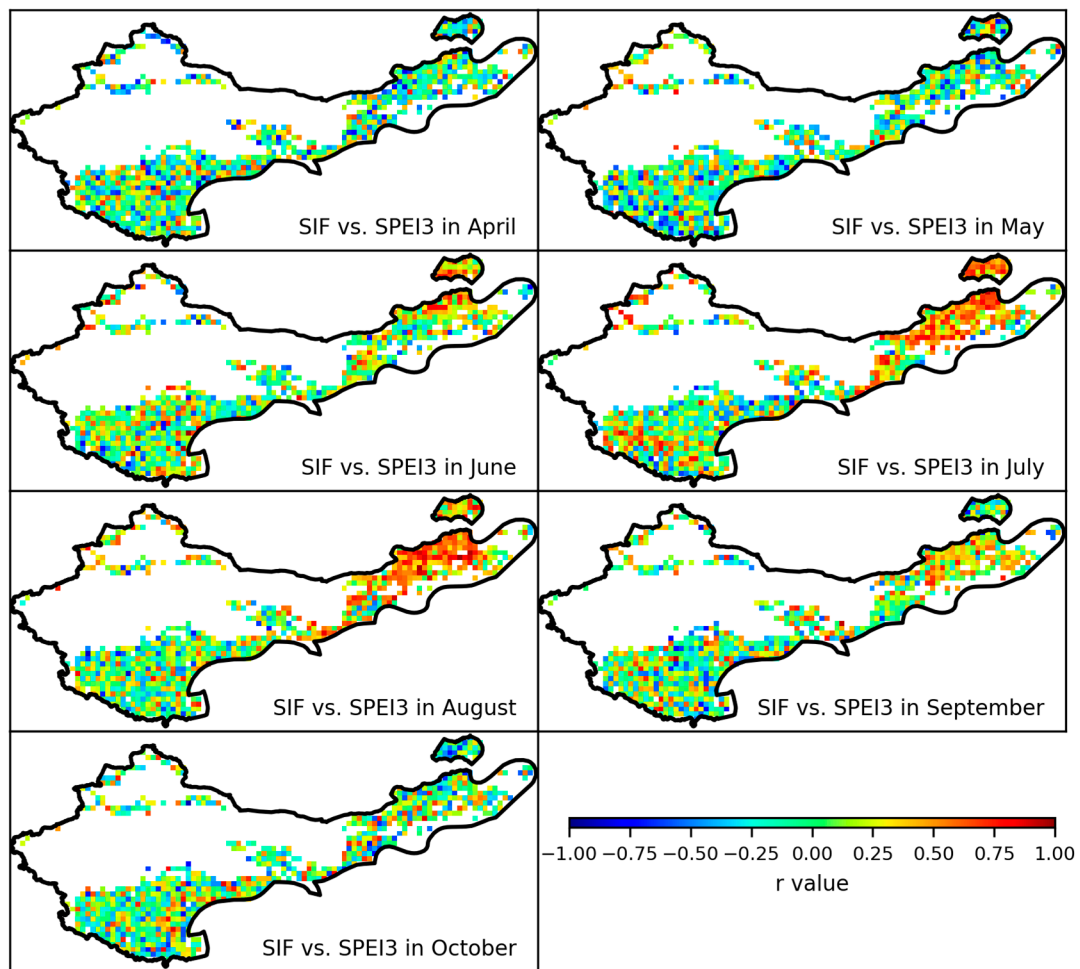


**Figure 3.** Spatiotemporal distribution of the correlation coefficients between SIF and three-month SPEI (SPEI-3) time scale. Pixels with white color mean non-grassland or missing data.

### 3.2. Spatiotemporal Pattern of Relationships between SIF and Different Drought Variables

In addition, the relationship between SIF and other variables was compared except SPEI, specifically PDSI, soil moisture, TCI, and VPD. Each record in Figure 4 is the  $r$  value between SIF and PDSI, SM, TCI, or VPD for one grid cell. For each grid cell, correlation analysis was performed taking SIF and one certain drought variable between 2007 and 2018 as the  $x$  and  $y$  variable, respectively. All the presented correlation coefficients in Figure 4 are statistically significant ( $p$  values  $< 0.05$ ). Generally, there were much stronger positive correlations between SIF and soil moisture than the correlations between SIF and TCI, VPD, and PDSI. The average correlation coefficients between SIF and soil moisture was 0.72 for the temperate grasslands and was 0.69 for the alpine grasslands. The average correlation coefficients between SIF and PDSI, TCI, VPD were 0.43, 0.38, and 0.39 for the temperate grasslands, and 0.39, 0.38, and 0.40 for the alpine grasslands, respectively. For soil moisture and PDSI, the correlation coefficients increased from April to August, and then decreased from July to October. For TCI and VPD, the medium of correlation coefficients ranged from 0.1 to 0.3, and there was no seasonal trend for the correlation coefficients.

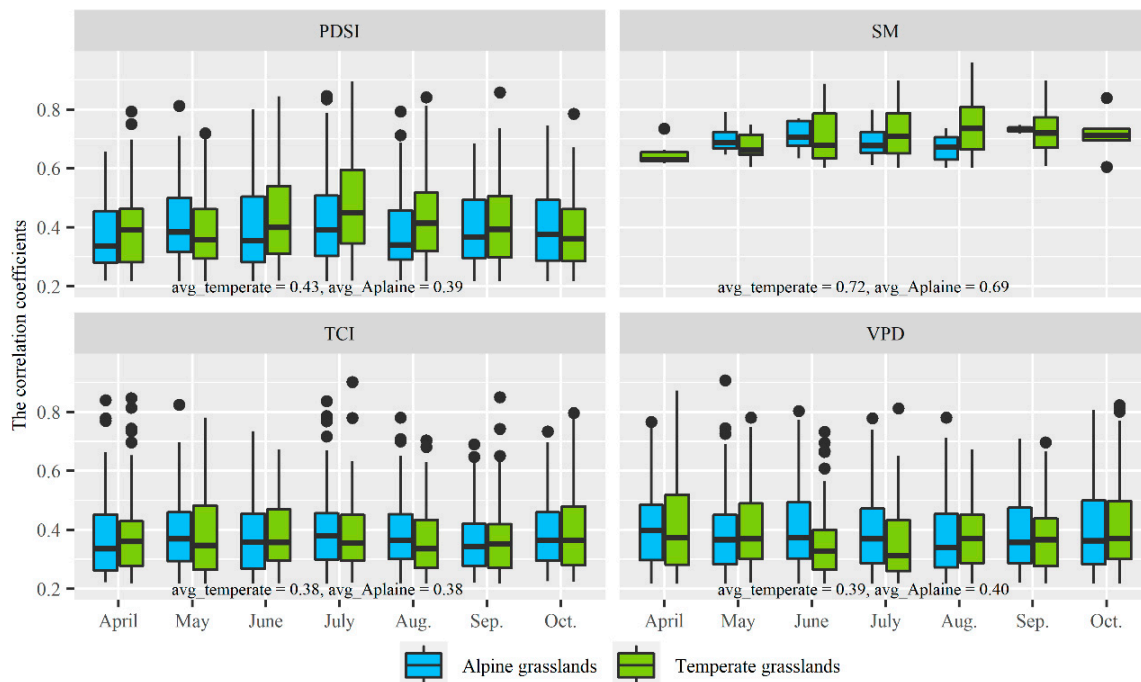


**Figure 4.** Correlation coefficients between SIF and (a) Palmer drought severity index PDSI, (b) soil moisture, (c) temperature condition index (TCI), and (d) vapor pressure deficit (VPD) for temperate grasslands and alpine grasslands. All the reported correlation coefficients are statistically significant ( $p$  values  $< 0.05$ ).

Over the study area, the spatial variabilities of the relationships between spaceborne SIF and drought variables are shown in Figure 5. The correlation between SIF and PDSI were stronger from June to August for temperate grasslands than alpine grasslands. While in April, May, September, and October, there were no differences between the temperate grasslands and alpine grasslands in terms of the relationship between SIF and PDSI. However, in July and August, the correlation coefficients between SIF and PDSI were higher than 0.5 for many pixels, especially for temperate grasslands, whereas for the alpine grasslands, the correlation coefficients between SIF and PDSI only show higher values in July.

The spatial and seasonal pattern of the correlation between SIF and soil moisture was similar to that between SIF and PDSI (Figure 6). The blank spaces are larger in Figure 6, because there were more missing data for the soil moisture data, especially in April, May, and October. The correlation coefficients of more than 36% of the pixels exceeded 0.6 in July and August.

For the correlation coefficients between SIF and VPD, and between SIF and TCI, many pixels showed negative values. The difference between temperate grasslands and alpine grasslands was not significant for all the months during the growing season. Generally, the correlation coefficients between SIF and TCI, and VPD were lower than between SIF and soil moisture, SPEI, and PDSI. Furthermore, there was no seasonal trend for the correlation coefficients between SIF and TCI and VPD (Figures 7 and 8).

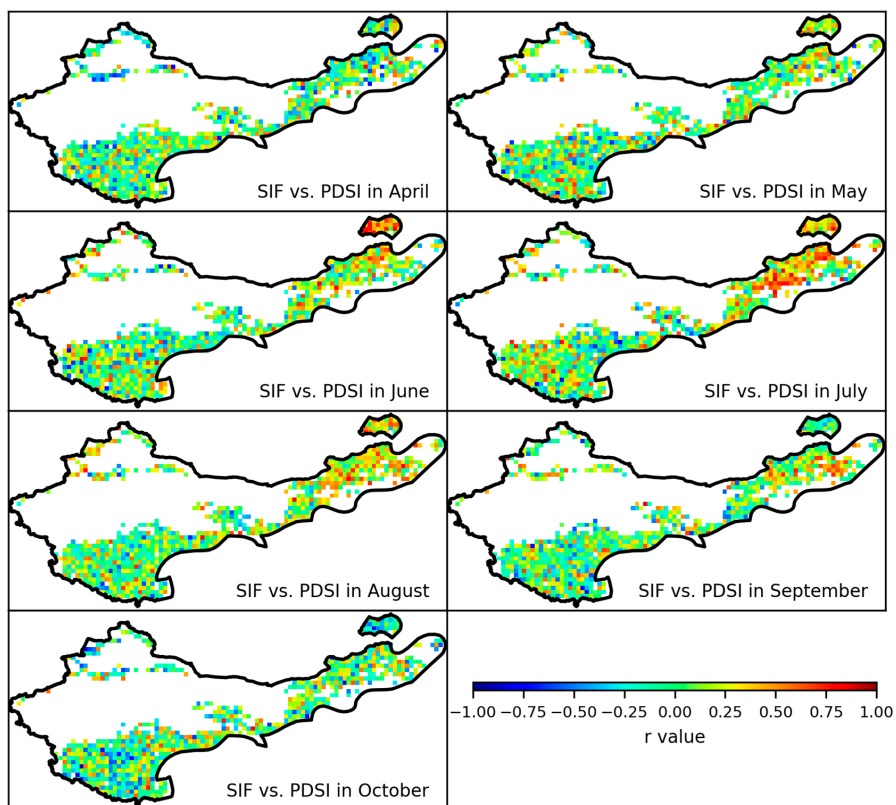


**Figure 5.** Spatiotemporal distribution of the correlation coefficients between SIF and PDSI in each month of growing season. Pixels with white color mean non-grassland or missing data.

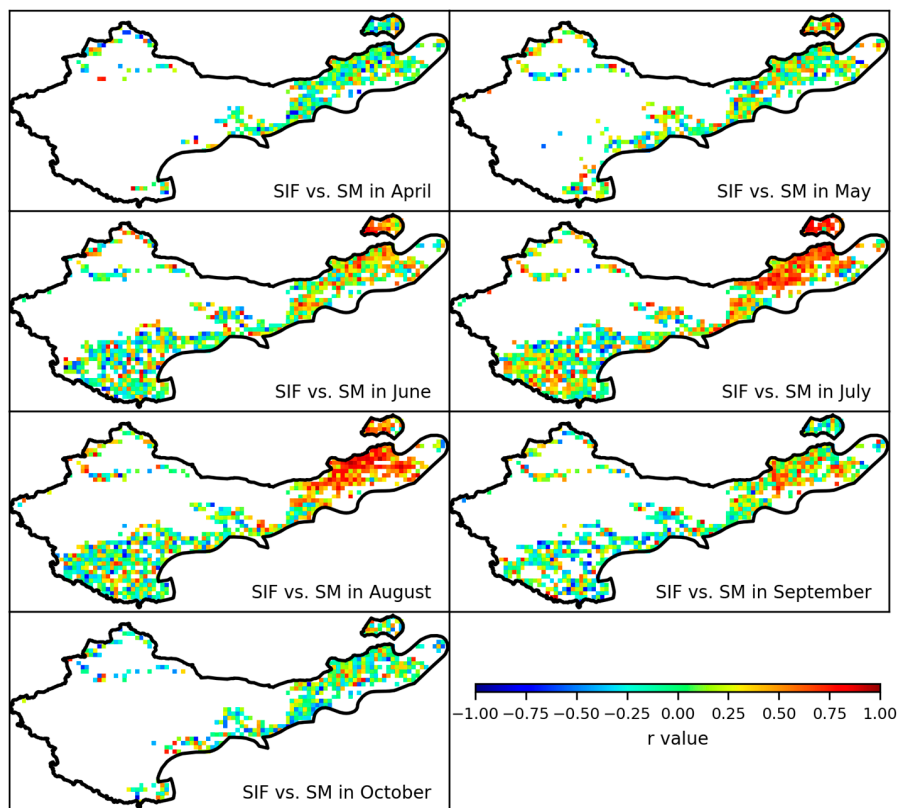


**Figure 6.** Spatiotemporal distribution of the correlation coefficients between SIF and soil moisture (SM) in each month of growing season. Pixels with white color mean non-grassland or missing data.

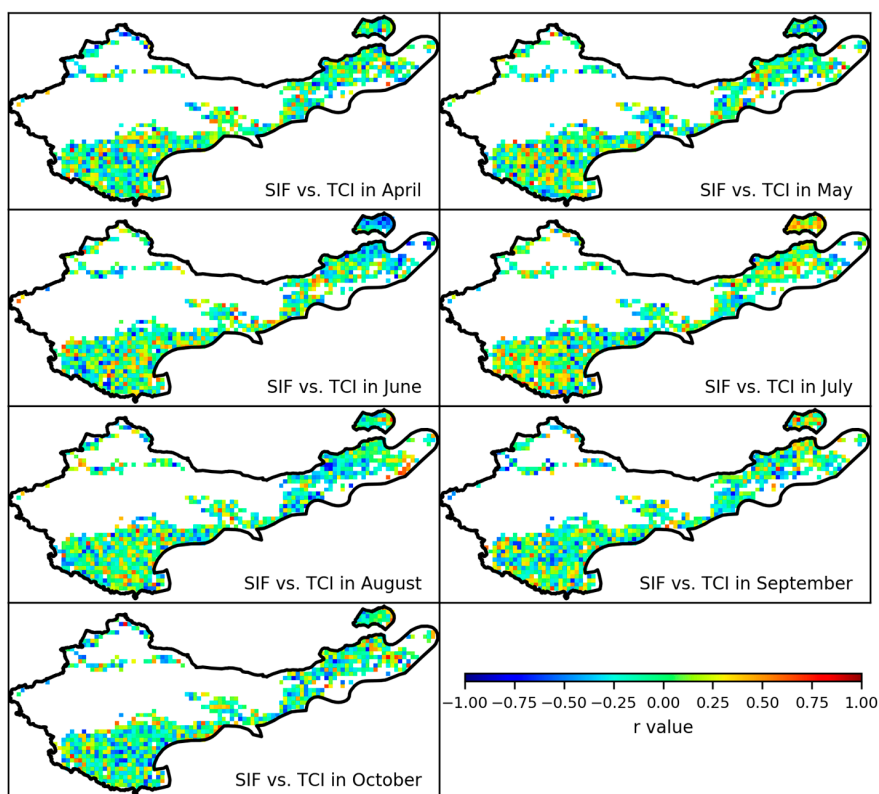


**Figure 7.** Spatiotemporal distribution of the correlation coefficients between SIF and TCI in each month of growing season. Pixels with white color mean non-grassland or missing data.

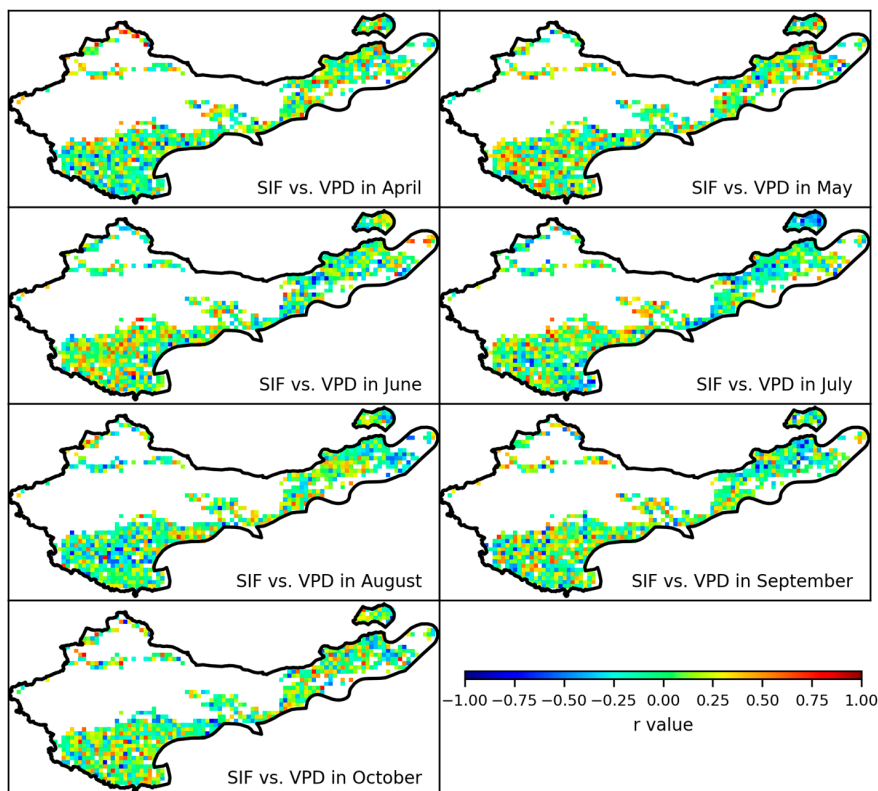


**Figure 8.** Spatiotemporal distribution of the correlation coefficients between SIF and VPD in each month of growing season. Pixels with white color mean non-grassland or missing data.

### 3.3. Regional Scale Comparison of Correlations between SIF and Different Drought Variables

At a regional scale, the correlation coefficients of SIF and the other nine drought variables across the arid and semiarid region for temperate grasslands and alpine grasslands are shown in Figures 9 and 10, respectively. For the temperate grasslands, SIF had the highest correlation coefficient with soil moisture in July ( $r = 0.52$ ), followed by SPEI-3 in July ( $r = 0.49$ ). The correlation coefficients between SIF and TCI and the correlation coefficients between SIF and VPD were generally lower than that with soil moisture, SPEIs, and PDSI.

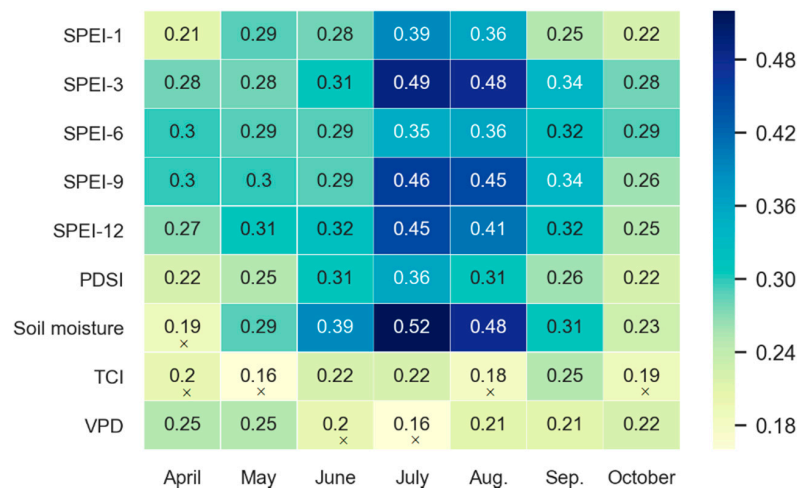


**Figure 9.** Comparison of the correlation coefficients between SIF and drought variables in each month of growing season for temperate grasslands. The symbol × represent significant correlations ( $0.01 < P < 0.05$ ). The correlation without symbol × were significant at 1% level.



**Figure 10.** Comparison of the correlation coefficients between SIF and drought variables in each month of growing season for alpine grasslands. The symbol × represent significant correlations ( $0.01 < P < 0.05$ ). The correlation without symbol × were significant at 1% level.

### 3.4. Driving Factors of the Variability in the Relationship between SIF and Drought Variables

To investigate the driving factors of the difference in the sensitivity of satellite SIF to drought variables, eight potential forces were investigated based on the RF regression method. We mainly studied the correlations between SIF and SPEI-3 ( $R_{SIF\_SPEI}$ ), between SIF and PDSI ( $R_{SIF\_PDSI}$ ), between SIF and soil moisture ( $R_{SIF\_SM}$ ), and between SIF and VPD ( $R_{SIF\_VPD}$ ) in July. The comparisons were made for July because the correlations between SIF and drought variables in July were stronger than

other months in general. According to the variable importance scores shown in Figure 11, the growing season mean temperature, minimum temperature, maximum temperature, and growing season mean radiation were shown to be dominant in the result, followed by DEM, LST, GPP, and precipitation. Similar to the  $R_{SIF\_SPEI}$ , temperature-related variables (minimum temperature, LST, mean temperature, and maximum temperature) were the most dominant driving forces for the spatial distribution of the  $R_{SIF\_PDSI}$ ,  $R_{SIF\_SM}$ , and  $R_{SIF\_VPD}$ . Mean growing season precipitation and GPP were the less important factors affecting the strength of  $R_{SIF\_PDSI}$ ,  $R_{SIF\_SM}$ , and  $R_{SIF\_VPD}$ . The results indicate that temperature variations will affect the sensitivity of grassland vegetation to drought.

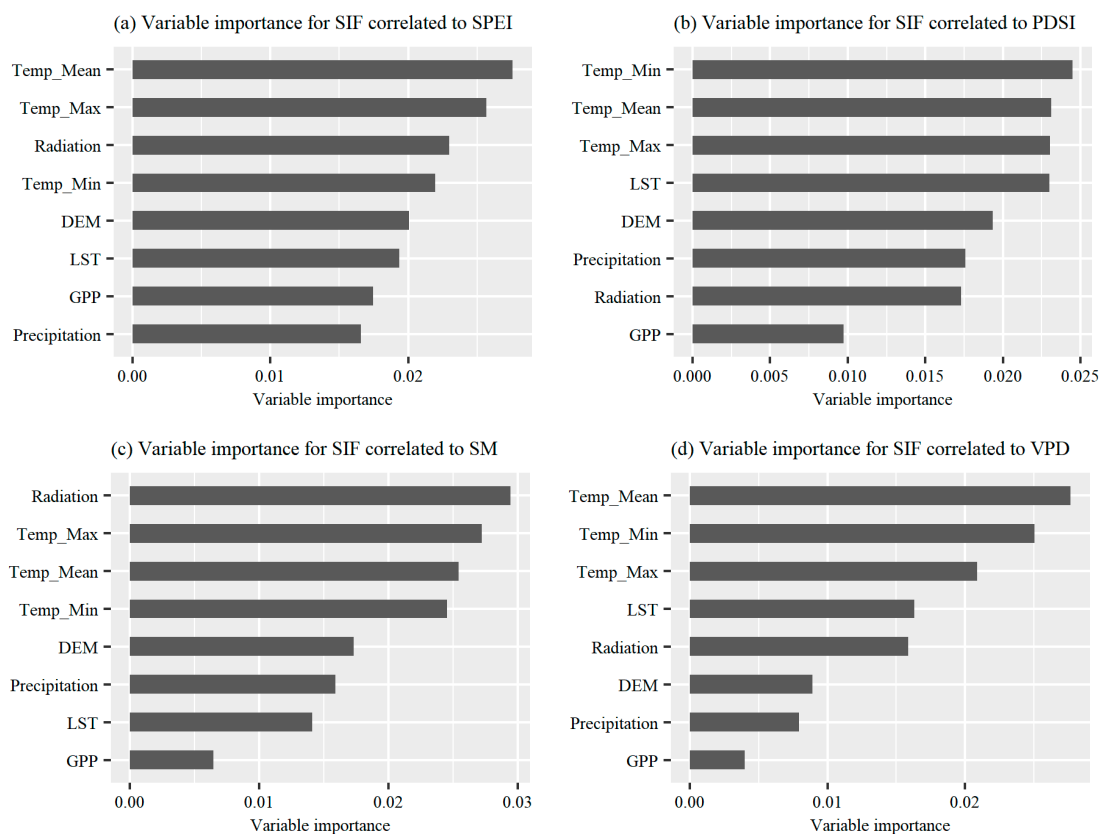


**Figure 11.** Importance of the eight factors for interpreting the correlation between satellite SIF and (a) SPEI, (b) PDSI, (c) SM, and (d) VPD. Temp\_Mean, Temp\_Max, Temp\_min, and LST represent the mean temperature, maximum temperature, minimum temperature, land surface temperature, respectively.

## 4. Discussion

### 4.1. Relationship between SIF and Different Drought Variables

Generally, the correlation coefficients between SIF and drought variables are relatively low. There are several reasons, for example, the processes and algorithms of SIF retrieval are complicated, and may contain some uncertainties. The coarse spatial and temporal resolution increased these uncertainties. This is similar to previous studies. For example, Chen et al. found that the correlation coefficients between SIF and SPEI, soil moisture, LST, precipitation were between  $-0.4$  and  $0.5$  over the North China Plain [35]. Jiao et al. calculated the correlation coefficients between SIF and meteorological drought indices for different ecosystem types in the continental United States, and the reported medians of the statistically significant correlation coefficients between grass SIF and drought indices were around  $0.5$  [1]. The correlations between SIF and soil moisture, SPEI, and PDSI were much stronger than other variables. In contrast, the correlation coefficient between SIF and TCI was the lowest. The results can be explained by the characteristics of the arid and semiarid climate zone. SPEI can account for

meteorological drought calculated from precipitation and potential evapotranspiration, while PDSI represents the balance of precipitation, potential evapotranspiration and temperature. However, TCI is derived solely based on temperature data. In the arid and semiarid zone, other than temperature, water condition is the dominant force accounting for the variance of vegetation growth. Therefore, the SIF was less sensitive to TCI than other drought variables. The VPD was calculated from the GLDAS NOAA temperature and vapor pressure, with a spatial resolution of 1°. The weak correlation between SIF and the VPD may primarily be due to the noise in the VPD data caused by the coarse spatial resolution, and it could not capture the localized information in space. In addition, the coarse temporal resolution (monthly time step) of the data also led to the weak correlation.

Furthermore, the results show that SIF has weaker correlations with SPEI-1 than SPEI under other time scales, because changes in the grass growth could be buffered by soil moisture. Drought condition does not inevitably lead to vegetation water pressure immediately. In some cases, when the early stage of drought occurs, plants could still take up moisture from the soil to maintain normal growth without suffering water deficiency for a period. The hydraulic redistribution effect of roots such as the water compensation capacity, can prevent or alleviate the harm of drought [52,53]. How long the grassland can withstand water storage depend on many factors, such as soil properties, grass species, and drought degree. This result is similar to previous studies [1,54]. The study performed in continental United States also showed that grassland SIF has the strongest correlation with SPEI-3 and longer-term drought did not significantly change grassland SIF sensitivity [1].

#### 4.2. Variance of SIF Response to Drought in the Two Grassland Ecosystem Types

The results demonstrated that temperate grasslands and alpine grasslands have different SIF sensitivity to drought variables. The magnitude and seasonality of the correlation coefficients between SIF and drought indices are different for temperate grasslands and alpine grasslands. Generally, SIF was more sensitive to drought for temperate grassland than alpine grassland. The temperate grasslands in the arid and semiarid zones are water limited. Therefore, the soil water deficit hinders vegetation growth by means of reducing the plant maximum photosynthetic rate [41]. Permafrost is a primary water source for the alpine grasslands, so the sensitivity of vegetation growth to drought was weaker in alpine grasslands [55]. The carbon and water cycle mechanisms for temperate grasslands and alpine grasslands are also different [56]. The results of RF regression revealed that climatic factors, topographic characteristics, and radiation could influence the ability of SIF to monitor drought. The high sensitivity of SIF to drought for temperate grasslands in arid and semiarid zones supports recent studies [1,26]. Xu et al. [26] found that the highest sensitivity of SIF to drought is particularly agro-pastoral ecotones in semiarid regions, which is consistent with high SIF sensitivity in this study.

For the alpine grasslands, more grid cells showed a negative correlation between SIF and drought variables than the temperate grasslands. The negative correlation means that drought events, such as a rise in temperature or a decrease in precipitation, could also increase the SIF signal in certain areas. The negative correlations in alpine grasslands are likely due to soil water not lacking when the drought occurs [57]. Sometimes when droughts occur, the temperature is high and the sky is clear, and the increased temperature and PAR may also increase the SIF value. Additionally, in some regions the heterogeneous pattern of positive and negative correlations could be attributed to the data quality. Negative SIF SPEI correlations were also observed in previous studies [26], which were likely caused by changes in leaf phenology and radiation limitation [58]. The RF regression analysis in this study also demonstrated that radiation was one of the important determinants for the sensitivity of SIF to drought.

#### 4.3. SIF Sensitivity in Different Stages during the Growing Season

The results indicate that the correlations of SIF to SPEIs, PDSI, and soil moisture during July and August were much higher than that in other months for temperate grasslands. For alpine grasslands, the correlations during June and July were higher. Model simulations also showed that the

seasonal photosynthesis responses of these two grassland types to climatic variation were different [30]. The weaker correlation between SIF and the drought variables in the early and late growing season may also be due to the sparse coverage of plants during these periods. Xu et al. also found that the intra-annual variation of spatially averaged OCO-2-based SIF was close to the normal distribution in northern China, and the averaged SIF in April, May, and October was much lower than that in June, July and August [26]. SIF data were lacking for many grid cells with low vegetation coverage in these months of the early and late growing season. The data quality could not reflect the vegetation variation reasonably and finally caused statistical uncertainties. Future studies can apply other sensors that have finer spatial resolution and temporal frequency, such as GeoCARB [59], TROPOMI [60], and FLEX [61]. In addition, some spatial downscaling algorithms have been developed to downscale satellite SIF data to a finer resolution [32,62].

There were several limitations in this study. First, the response of SIF to drought was assessed using correlation analysis. Correlation relationships do not certainly denote causation relationships. Second, the current applied SIF data have a coarse spatial resolution of 0.5°, and detailed spatial information could not be captured soundly. Third, the time series are short and cover 12 years only (the period from 2007 to 2018). Recently, Li and Xiao [63] developed a SIF data set over the period 2000–2017 based on discrete OCO-2 SIF soundings, MODIS data, and meteorological data, which could be used in future research.

## 5. Conclusions

This study examined the characteristics of spaceborne SIF correlations to drought variables in arid and semiarid regions from 2007 to 2018 for two typical grassland ecosystems. We found that the correlation coefficient between SIF and soil moisture was the strongest, followed by SPEI and PDSI, while the correlation coefficient between SIF and TCI was the weakest. For this arid and semiarid region, we also found that the temperate grassland SIF demonstrated higher sensitivity to drought than alpine grassland SIF, and more negative correlations were found in alpine grasslands than temperate grasslands. Generally, the response of SIF to drought was more pronounced during the peak period of the growing season than during the early and late growing season. Among the climatic factors, DEM, GPP, growing season temperature factors and radiation are the most important variables for the correlation of SIF to the drought variables. Spaceborne SIF has great potential to detect drought for temperate grasslands during the peak growing season in arid and semiarid zones. It should be noted that this research explored the responses of satellite SIF to drought from a statistic perspective; in future, field SIF measurements should also be performed to provide more information about the mechanisms.

**Author Contributions:** Conceptualization, Meng Wang; Data curation, Guicai Li; Formal analysis, Xiaofang Sun; Funding acquisition, Junbang Wang; Methodology, Xiaofang Sun and Zemeng Fan; Resources, Guicai Li; Supervision, Meng Wang; Validation, Meng Wang; Writing—original draft, Xiaofang Sun; Writing—review and editing, Meng Wang and Junbang Wang. All authors have read and agreed to the published version of the manuscript.

**Funding:** This research was funded by the National Natural Science Foundation of China (grant no. 31861143015, 41501428, 41371400), the National Key Research and Development Program of China (grant no. 2016YFA0600204), and a grant from State Key Laboratory of Resources and Environmental Information System.

**Conflicts of Interest:** The authors declare no conflict of interest.

## References

1. Jiao, W.; Chang, Q.; Wang, L. The sensitivity of satellite solar-induced chlorophyll fluorescence to meteorological drought. *Earths Future* **2019**, *7*, 558–573. [[CrossRef](#)]
2. Feng, W.; Shum, C.K.; Zhong, M.; Pan, Y. Groundwater storage changes in China from satellite gravity: An overview. *Remote Sens.* **2018**, *10*, 674. [[CrossRef](#)]
3. Hellwig, J.; de Graaf, I.E.M.; Weiler, M.; Stahl, K. Large-scale assessment of delayed groundwater responses to drought. *Water Resour. Res.* **2020**, *56*, e2019WR025441. [[CrossRef](#)]

4. Liu, X.; Pan, Y.; Zhu, X.; Yang, T.; Bai, J.; Sun, Z. Drought evolution and its impact on the crop yield in the North China Plain. *J. Hydrol.* **2018**, *564*, 984–996. [[CrossRef](#)]
5. Jamshidi, S.; Zand-Parsa, S.; Kamgar-Haghighi, A.A.; Shahsavari, A.R.; Niyogi, D. Evapotranspiration, crop coefficients, and physiological responses of citrus trees in semi-arid climatic conditions. *Agric. Water Manag.* **2020**, *227*, 105838. [[CrossRef](#)]
6. He, W.; Ju, W.; Schwalm, C.; Sippel, S.; Wu, X.; Qiaoning, H.; Song, L.; Zhang, C.; Li, J.; Sitch, S.; et al. Large-scale droughts responsible for dramatic reductions of terrestrial net carbon uptake over North America in 2011 and 2012. *J. Geophys. Res. Biogeosci.* **2018**, *123*, 2053–2071. [[CrossRef](#)]
7. Yu, C.; Huang, X.; Chen, H.; Huang, G.; Ni, S.; Wright, J.S.; Hall, J.; Ciais, P.; Zhang, J.; Xiao, Y.; et al. Assessing the impacts of extreme agricultural droughts in China under climate and socioeconomic changes. *Earths Future* **2018**, *6*, 689–703. [[CrossRef](#)]
8. Li, X.; Li, Y.; Chen, A.; Gao, M.; Slette, I.J.; Piao, S. The impact of the 2009/2010 drought on vegetation growth and terrestrial carbon balance in southwest china. *Agric. For. Meteorol.* **2019**, *269*, 239–248. [[CrossRef](#)]
9. Zhang, X.; Chen, N.; Li, J.; Chen, Z.; Niyogi, D. Multi-sensor integrated framework and index for agricultural drought monitoring. *Remote Sens. Environ.* **2017**, *188*, 141–163. [[CrossRef](#)]
10. Wang, J.; Dong, J.; Yi, Y.; Lu, G.; Oyler, J.; Smith, W.; Zhao, M.; Liu, J.; Running, S. Decreasing net primary production due to drought and slight decreases in solar radiation in China from 2000 to 2012. *J. Geophys. Res. Biogeosci.* **2017**, *112*, 261–278. [[CrossRef](#)]
11. Alamdarloo, E.H.; Manesh, M.B.; Khosravi, H. Probability assessment of vegetation vulnerability to drought based on remote sensing data. *Environ. Monitor. Assess.* **2018**, *190*, 702. [[CrossRef](#)] [[PubMed](#)]
12. Chang, C.; Wang, H.; Huang, C. Assessment of modis-derived indices (2001–2013) to drought across taiwan's forests. *Int. J. Biometeorol.* **2017**, *62*, 809–822. [[CrossRef](#)] [[PubMed](#)]
13. Bajgain, R.; Xiao, X.; Wagle, P.; Basara, J.; Zhou, Y. Sensitivity analysis of vegetation indices to drought over two tallgrass prairie sites. *ISPRS J. Photogramm. Remote Sens.* **2015**, *108*, 151–160. [[CrossRef](#)]
14. Yoshida, Y.; Joiner, J.; Tucker, C.; Berry, J.; Lee, J.E.; Walker, G.; Reichle, R.; Koster, R.; Lyapustin, A.; Wang, Y. The 2010 russian drought impact on satellite measurements of solar-induced chlorophyll fluorescence: Insights from modeling and comparisons with parameters derived from satellite reflectances. *Remote Sens. Environ.* **2015**, *166*, 163–177. [[CrossRef](#)]
15. Jeong, S.-J.; Schimel, D.; Frankenberg, C.; Drewry, D.T.; Fisher, J.B.; Verma, M.; Berry, J.A.; Lee, J.-E.; Joiner, J. Application of satellite solar-induced chlorophyll fluorescence to understanding large-scale variations in vegetation phenology and function over northern high latitude forests. *Remote Sens. Environ.* **2017**, *190*, 178–187. [[CrossRef](#)]
16. Koehler, P.; Guanter, L.; Kobayashi, H.; Walther, S.; Yang, W. Assessing the potential of sun-induced fluorescence and the canopy scattering coefficient to track large-scale vegetation dynamics in amazon forests. *Remote Sens. Environ.* **2018**, *204*, 769–785. [[CrossRef](#)]
17. Lu, X.; Liu, Z.; Zhou, Y.; Liu, Y.; An, S.; Tang, J. Comparison of phenology estimated from reflectance-based indices and solar-induced chlorophyll fluorescence (sif) observations in a temperate forest using gpp-based phenology as the standard. *Remote Sens.* **2018**, *10*, 932. [[CrossRef](#)]
18. Ma, J.; Xiao, X.; Zhang, Y.; Doughty, R.; Chen, B.; Zhao, B. Spatial-temporal consistency between gross primary productivity and solar-induced chlorophyll fluorescence of vegetation in china during 2007–2014. *Sci. Total Environ.* **2018**, *639*, 1241–1253. [[CrossRef](#)]
19. Wang, X.; Qiu, B.; Li, W.; Zhang, Q. Impacts of drought and heatwave on the terrestrial ecosystem in china as revealed by satellite solar-induced chlorophyll fluorescence. *Sci. Total Environ.* **2019**, *693*, 133627. [[CrossRef](#)]
20. Zhang, L.; Qiao, N.; Huang, C.; Wang, S. Monitoring drought effects on vegetation productivity using satellite solar-induced chlorophyll fluorescence. *Remote Sens.* **2019**, *11*, 378. [[CrossRef](#)]
21. Sun, Y.; Fu, R.; Dickinson, R.; Joiner, J.; Frankenberg, C.; Gu, L.; Xia, Y.; Fernando, N. Drought onset mechanisms revealed by satellite solar-induced chlorophyll fluorescence: Insights from two contrasting extreme events. *J. Geophys. Res.-Biogeosci.* **2015**, *120*, 2427–2440. [[CrossRef](#)]
22. Lai, C.; Zhong, R.; Wang, Z.; Wu, X.; Chen, X.; Wang, P.; Lian, Y. Monitoring hydrological drought using long-term satellite-based precipitation data. *Sci. Total Environ.* **2019**, *649*, 1198–1208. [[CrossRef](#)] [[PubMed](#)]
23. Sharma, S.; Mujumdar, P. Increasing frequency and spatial extent of concurrent meteorological droughts and heatwaves in india. *Sci. Rep.* **2017**, *7*, 1–9. [[CrossRef](#)] [[PubMed](#)]

24. Jamshidi, S.; Zand-Parsa, S.; Jahromi, M.N.; Niyogi, D. Application of a simple landsat-modis fusion model to estimate evapotranspiration over a heterogeneous sparse vegetation region. *Remote Sens.* **2019**, *11*, 741. [[CrossRef](#)]
25. Jamshidi, S.; Zand-parsa, S.; Pakparvar, M.; Niyogi, D. Evaluation of evapotranspiration over a semiarid region using multiresolution data sources. *J. Hydrometeorol.* **2019**, *20*, 947–964. [[CrossRef](#)]
26. Xu, H.; Wang, X.; Zhao, C.; Yang, X. Assessing the response of vegetation photosynthesis to meteorological drought across Northern China. *Land Degrad. Dev.* **2020**. [[CrossRef](#)]
27. Sun, X.; Wang, M.; Li, G.; Wang, Y. Regional-scale drought monitor using synthesized index based on remote sensing in northeast china. *Open Geosci.* **2020**, *12*, 163. [[CrossRef](#)]
28. Li, Z.; Han, Y.; Hao, T. Assessing the consistency of remotely sensed multiple drought indices for monitoring drought phenomena in continental China. *IEEE Trans. Geosci. Remote Sens.* **2020**, *58*, 5490–5502. [[CrossRef](#)]
29. Sanders, A.F.J.; Verstraeten, W.W.; Kooreman, M.L.; van Leth, T.C.; Beringer, J.; Joiner, J. Spaceborne sun-induced vegetation fluorescence time series from 2007 to 2015 evaluated with australian flux tower measurements. *Remote Sens.* **2016**, *8*, 895. [[CrossRef](#)]
30. Wang, S.; Huang, C.; Zhang, L.; Lin, Y.; Cen, Y.; Wu, T. Monitoring and assessing the 2012 drought in the great plains: Analyzing satellite-retrieved solar-induced chlorophyll fluorescence, drought indices, and gross primary production. *Remote Sens.* **2016**, *8*, 61. [[CrossRef](#)]
31. Zhang, Y.; Xiao, X.; Jin, C.; Dong, J.; Zhou, S.; Wagle, P.; Joiner, J.; Guanter, L.; Zhang, Y.; Zhang, G.; et al. Consistency between sun-induced chlorophyll fluorescence and gross primary production of vegetation in north america. *Remote Sens. Environ.* **2016**, *183*, 154–169. [[CrossRef](#)]
32. Duveiller, G.; Cescatti, A. Spatially downscaling sun-induced chlorophyll fluorescence leads to an improved temporal correlation with gross primary productivity. *Remote Sens. Environ.* **2016**, *182*, 72–89. [[CrossRef](#)]
33. Geruo, A.; Velicogna, I.; Kimball, J.S.; Du, J.; Kim, Y.; Njoku, E. Satellite-observed changes in vegetation sensitivities to surface soil moisture and total water storage variations since the 2011 texas drought. *Environ. Res. Lett.* **2017**, *12*, 054006.
34. Ni, Z.; Huo, H.; Tang, S.; Li, Z.-L.; Liu, Z.; Xu, S.; Chen, B. Assessing the response of satellite sun-induced chlorophyll fluorescence and modis vegetation products to soil moisture from 2010 to 2017: A case in yunnan province of china. *Int. J. Remote Sens.* **2019**, *40*, 2278–2295. [[CrossRef](#)]
35. Chen, X.; Mo, X.; Zhang, Y.; Sun, Z.; Liu, Y.; Hu, S.; Liu, S. Drought detection and assessment with solar-induced chlorophyll fluorescence in summer maize growth period over north china plain. *Ecol. Indic.* **2019**, *104*, 347–356. [[CrossRef](#)]
36. Qian, X.; Qiu, B.; Zhang, Y. Widespread decline in vegetation photosynthesis in southeast asia due to the prolonged drought during the 2015/2016 el nino. *Remote Sens.* **2019**, *11*, 910. [[CrossRef](#)]
37. Merrick, T.; Pau, S.; Jorge, M.L.S.P.; Silva, T.S.F.; Bennartz, R. Spatiotemporal patterns and phenology of tropical vegetation solar-induced chlorophyll fluorescence across brazilian biomes using satellite observations. *Remote Sens.* **2019**, *11*, 1746. [[CrossRef](#)]
38. Mao, D.; Wang, Z.; Wu, B.; Zeng, Y.; Luo, L.; Zhang, B. Land degradation and restoration in the arid and semiarid zones of china: Quantified evidence and implications from satellites. *Land Degrad. Dev.* **2018**, *29*, 3841–3851. [[CrossRef](#)]
39. Xu, C.; Liu, H.; Williams, A.P.; Yin, Y.; Wu, X. Trends toward an earlier peak of the growing season in northern hemisphere mid-latitudes. *Glob. Chang. Biol.* **2016**, *22*, 2852–2860. [[CrossRef](#)]
40. Xiangjin, S.; Zhou, D.; Li, F.; Zhang, H. Vegetation change and its response to climate change in grassland region of china. *Sci. Geogr. Sin.* **2015**, *35*, 622–629.
41. Yang, J.; Dong, J.; Xiao, X.; Dai, J.; Wu, C.; Xia, J.; Zhao, G.; Zhao, M.; Li, Z.; Zhang, Y.; et al. Divergent shifts in peak photosynthesis timing of temperate and alpine grasslands in china. *Remote Sens. Environ.* **2019**, *233*, 111395. [[CrossRef](#)]
42. Guan, K.; Berry, J.A.; Zhang, Y.; Joiner, J.; Guanter, L.; Badgley, G.; Lobell, D.B. Improving the monitoring of crop productivity using spaceborne solar-induced fluorescence. *Glob. Chang. Biol.* **2016**, *22*, 716–726. [[CrossRef](#)] [[PubMed](#)]
43. Joiner, J.; Yoshida, Y.; Guanter, L.; Middleton, E.M. New methods for the retrieval of chlorophyll red fluorescence from hyperspectral satellite instruments: Simulations and application to gome-2 and sciamachy. *Atmos. Meas. Tech.* **2016**, *9*, 3939–3967. [[CrossRef](#)]

44. Vicente-Serrano, S.M.; Azorin-Molina, C.; Pena-Gallardo, M.; Tomas-Burguera, M.; Dominguez-Castro, F.; Martin-Hernandez, N.; Begueria, S.; El Kenawy, A.; Noguera, I.; Garcia, M. A high-resolution spatial assessment of the impacts of drought variability on vegetation activity in Spain from 1981 to 2015. *Nat. Hazards Earth Syst. Sci.* **2019**, *19*, 1189–1213. [[CrossRef](#)]
45. Dai, A. Drought under global warming: A review. *Wiley Interdiscip. Rev.-Clim. Chang.* **2011**, *2*, 45–65. [[CrossRef](#)]
46. Wang, H.; He, B.; Zhang, Y.; Huang, L.; Chen, Z.; Liu, J. Response of ecosystem productivity to dry/wet conditions indicated by different drought indices. *Sci. Total Environ.* **2018**, *612*, 347–357. [[CrossRef](#)] [[PubMed](#)]
47. Gruber, A.; Scanlon, T.; van der Schalie, R.; Wagner, W.; Dorigo, W. Evolution of the ESA CCI soil moisture climate data records and their underlying merging methodology. *Earth Syst. Sci. Data* **2019**, *11*, 717–739. [[CrossRef](#)]
48. Dorigo, W.; Wagner, W.; Albergel, C.; Albrecht, F.; Balsamo, G.; Brocca, L.; Chung, D.; Ertl, M.; Forkel, M.; Gruber, A.; et al. ESA CCI soil moisture for improved Earth system understanding: State-of-the-art and future directions. *Remote Sens. Environ.* **2017**, *203*, 185–215. [[CrossRef](#)]
49. Gruber, A.; Dorigo, W.A.; Crow, W.; Wagner, W. Triple collocation-based merging of satellite soil moisture retrievals. *IEEE Trans. Geosci. Remote Sens.* **2017**, *55*, 6780–6792. [[CrossRef](#)]
50. Sun, X.; Li, B.; Du, Z.; Li, G.; Fan, Z.; Wang, M.; Yue, T. Surface modelling of forest aboveground biomass based on remote sensing and forest inventory data. *Geocarto Int.* **2019**, 1–16. [[CrossRef](#)]
51. Liaw, A.; Wiener, M. Classification and regression by random forest. *R News* **2002**, *23*, 18–22.
52. Javaux, M.; Schroeder, T.; Vanderborght, J.; Vereecken, H. Use of a three-dimensional detailed modeling approach for predicting root water uptake. *Vadose Zone J.* **2008**, *7*, 1079–1088. [[CrossRef](#)]
53. Zou, H.; Gao, G.; Fu, B. The relationship between grassland ecosystem and soil water in arid and semi-arid areas: A review. *Acta Ecol. Sin.* **2016**, *36*, 3127–3136.
54. Quiring, S.M.; Ganesh, S. Evaluating the utility of the vegetation condition index (vci) for monitoring meteorological drought in Texas. *Agric. For. Meteorol.* **2010**, *150*, 330–339. [[CrossRef](#)]
55. Chen, H.; Zhu, Q.; Peng, C.; Wu, N.; Wang, Y.; Fang, X.; Gao, Y.; Zhu, D.; Yang, G.; Tian, J.; et al. The impacts of climate change and human activities on biogeochemical cycles on the Qinghai-Tibetan Plateau. *Glob. Chang. Biol.* **2013**, *19*, 2940–2955. [[CrossRef](#)]
56. Ge, R.; He, H.; Ren, X.; Zhang, L.; Li, P.; Zeng, N.; Yu, G.; Zhang, L.; Yu, S.-Y.; Zhang, F.; et al. A satellite-based model for simulating ecosystem respiration in the Tibetan and Inner Mongolian grasslands. *Remote Sens.* **2018**, *10*, 149. [[CrossRef](#)]
57. Wang, H.; Rogers, J.C.; Munroe, D.K. Commonly used drought indices as indicators of soil moisture in China. *J. Hydrometeorol.* **2015**, *16*, 1397–1408. [[CrossRef](#)]
58. Xu, H.; Zhao, C.; Wang, X. Spatiotemporal differentiation of the terrestrial gross primary production response to climate constraints in a dryland mountain ecosystem of Northwestern China. *Agric. For. Meteorol.* **2019**, 276–277, 107628. [[CrossRef](#)]
59. Buis, A. GeoCarb: A New View of Carbon over the Americas. Available online: <https://www.nasa.gov/feature/jpl/geocarb-a-new-view-of-carbon-over-the-americas> (accessed on 18 April 2019).
60. Köhler, P.; Frankenberg, C.; Magney, T.S.; Guanter, L.; Joiner, J.; Landgraf, J. Global retrievals of solar-induced chlorophyll fluorescence with TROPOMI: First results and intersensor comparison to OCO-2. *Geophys. Res. Lett.* **2018**, *45*, 456–463. [[CrossRef](#)]
61. Drusch, M.; Moreno, J.; Bello, U.D.; Franco, R.; Goulas, Y.; Huth, A.; Kraft, S.; Middleton, E.M.; Miglietta, F.; Mohammed, G.; et al. The fluorescence explorer mission concept—ESA's Earth Explorer 8. *IEEE Trans. Geosci. Remote Sens.* **2017**, *55*, 1273–1284. [[CrossRef](#)]
62. Badgley, G.; Field, C.B.; Berry, J.A. Canopy near-infrared reflectance and terrestrial photosynthesis. *Sci. Adv.* **2017**, *3*, e1602244. [[CrossRef](#)] [[PubMed](#)]
63. Li, X.; Xiao, J. A global, 0.05-degree product of solar-induced chlorophyll fluorescence derived from OCO-2, MODIS, and reanalysis data. *Remote Sens.* **2019**, *11*, 517. [[CrossRef](#)]

